Available online at https://link.springer.com/journal/42241
http://www.jhydrodynamics.com
Journal of Hydrodynamics, 2022
https://doi.org/10.1007/s42241-022-0051-2

Correlation analysis between underwater noise and Liutex for DTMB4119 propeller

Lian-jie Yu[1], Jian-wei Wu[2], De-cheng Wan[1*]
1. *Computational Marine Hydrodynamics Lab (CMHL), School of Naval Architecture, Ocean and Civil Engineering, Shanghai Jiao Tong University, Shanghai 200240, China*
2. *Wuhan Second Ship Design and Research Institute, Wuhan 430205, China*

(Received December 25, 2021, Revised April 10, 2022, Accepted April 11, 2022, Published online August 16, 2022)

Abstract: Propeller is an important equipment of ocean structures. It has characteristics of complex geometry and periodic vortex shed, which means high research value. This paper takes DTMB419 propeller as the research object. A detailed study is conducted on the wake vortices in non-cavitation state and cavitation state. Three vortex identification methods are used to compare the vortices capture effects from downstream sections and three-dimensional perspectives. The results show that, the third-generation vortex identification technology Ω_R shows obvious advantages. At the same time, FW-H equation is used to predict propeller noise, and the relationship between nonlinear sound source distribution and vortices distribution is analyzed. It is found that the distribution of Lighthill tensor is consistent with Ω_R, which proves the advantages and potential of third-generation vortex identification technology from acoustic perspective.

Key words: Third-generation vortex, DTMB4119 propeller, cavitation, FW-H formulation

Introduction

Turbulent flow is highly complex. Fluid viscosity induces eddies. The generation of vortices has an impact on the lift force, drag force, vibration and noise of structures. Accurate capture of vortex affects the calculation of forces and many other details of flow field. There are various fluid mechanics equations with eddy as a parameter, and they all explain problems in the flow field from the perspective of vortices[1]. These findings are difficult to obtain from traditional perspectives of velocity and pressure.

At first, the vortex is defined by the structure of the vortex line or vortex tube. Such method considers the vortex line or vortex tube to be equivalent to eddies. This technique is the concept of vorticity actually, and applied to the field of fluid mechanics. Vorticity is considered to be the first-generation vortex identification technology[2]. Since then, scholars proposed a series of vortex identification methods such as Q-criterion, λ_2 and so on. These techniques are all based on Cauthy-Stokes decomposition of velocity gradient tensors and are considered to be the second- generation vortex identification methods[3]. In 2014, the Eddy and Turbulence Research Team at the University of Texas at Arlington (UTA) developed a new vortex identification technique. They proposed a concept, Ω_R, which defines vortex as a connected region where the vorticity exceeds the deformation. Based on this, Prof. Chaoqun Liu proposed the third-generation vortex identification technology, Liutex[4]. It describes the position of the vortex core, the size of the vortex, the rotation axis, the absolute strength and the relative strength of vortex, which are difficult for traditional vortex identification methods[5].

The vortices system of propeller is complex, such as hub vortex and tip vortex. For high-speed rotating propellers, cavitation may occur underwater, and the interaction between cavitation and wake vortices enhances the fluctuation of turbulent flow. The accurate prediction of thrust and torque is inseparable from the reliable simulation of the flow field. And the precise capture of vortex affects the results of the flow

Project supported by the National Key Research and Development Program of China (Grant No. 2019YFB1704200), the National Natural Science Foundation of China (Grant Nos. 51909160, 52131102 and 51879159).
Biography: Lian-jie Yu (1993-), Male, Ph. D.,
E-mail: leo_yates@163.com
Corresponding author: De-cheng Wan,
E-mail: dcwan@sjtu.edu.cn

field. The first and second generation vortex identifications cause shear and false vortices near the boundary[6]. However, the third-generation vortex identification overcomes these problems[7].

Sound is the most effective signal traveling underwater. Noise affects a ship's stealth and the ability to detect enemies[8]. There are three main sources of ship noise: mechanical noise, propeller noise and flow noise. The flow noise becomes an important sound source when the ship is running at high speed. It also interferes with the sonar[9]. Therefore, it is necessary to study flow noise. The near field is considered to be caused by the pressure fluctuations. The time derivative of the near field pressure can be obtained by finite volume method (FVM) or others. For the far-field radiated noise, such method is unacceptable due to the high computational cost[10]. Therefore, Various models for far-field radiated noise emerged, the most important being Lighthill's acoustic analogy[11].

Lighthill transformed Navier-Stokes equation into the form of wave equation, and the terms related to nonlinearity are all regarded as the source terms of the wave equation[12-14]. Among them, quadrupoles are considered to be related to vortex. Therefore, accurate capturing of eddies is an important aspect of noise predictions. Assuming that the nonlinear effects all appear in the vicinity of the turbulent flow, the computational domain can be artificially divided into the near field and the far field. The source term of the wave equation is solved by computational fluid dynamics (CFD) methods in the near field, and the noise is predicted using a linear propagation model in the far field. Ianniello[15-16] used acoustic analogy to predict the underwater noise of a full-scale ship in steady flow. The results show that acoustic analogy behave well in both the direction and amplitude of noise predictions. Dottorale[17] employed Lighthill's idea, combined with the boundary element method (BEM), to compute the flow noise under open water. He compared the results with the unsteady Bernoulli equation in the potential flow theory. It is found that the results of acoustic analogy are more accurate. Lloyd et al.[18] used acoustic analogy to predict far-field noise, and compared the direct calculation method with the acoustic analogy. Studies show that convergent near-field CFD solutions are important for acoustic analogy.

1. Mathematical formulations

1.1 *Turbulence modelling*

The propeller wake problem is highly complex. In order to ensure the accuracy of noise calculation, this paper adopts the delayed detached-eddy simulation (DDES) turbulence model, more specifically, the improved Spalart-Allmaras detached-eddy simulation (DES), namely SA-DDES[19]. The governing equation is as follows

$$\frac{\partial\tilde{v}}{\partial t}+\nabla\cdot(\tilde{v}u)=\frac{1}{C_\sigma}\left\{\nabla\cdot\left[(v+\tilde{v})\nabla\tilde{v}\right]+C_{b2}\frac{\partial\tilde{v}}{\partial x_i}\frac{\partial\tilde{v}}{\partial x_j}\right\}+$$

$$C_{b1}\tilde{S}\tilde{v}-C_{w1}f_w\left(\frac{\tilde{v}}{\tilde{d}}\right)^2 \tag{1}$$

The first term on the left-hand side represents the transient term, and the second term is the convection term; the diffusion term is the first term on the right-hand side. the source term is the second term, and the dissipation term is the third term. The modified $\tilde{d}$ in the DDES equation is:

$$\tilde{d}=d_w-f_d\max(d_w-C_{\mathrm{DES}}\Delta,0) \tag{2}$$

$$f_d=1-\tanh[(8r_d)^3] \tag{3}$$

$$r_d=\frac{v_t+v}{\sqrt{U_{ij}U_{ij}}(\kappa d_w)^2} \tag{4}$$

1.2 *Cavitation model*

The cavitation model equation is derived from the Rayleigh-Plesset equation of the bubble dynamics equation. In the cavitation model, vaporization is regarded as a positive mass term, and liquefaction is regarded as a negative mass term. In this paper, the Schnerr-Sauer cavitation model[20] is adopted. Its mass conversion equation is as follows

$$\frac{\partial(\rho_v)}{\partial t}+\frac{\partial(\rho_v\alpha_v u_j)}{\partial x_j}=\dot{m}^+-\dot{m}^- \tag{5}$$

where α_v is the vapour volume fraction, the source terms $\dot{m}^+$ and $\dot{m}^-$ represent the evaporation and condensation processes, respectively. When the phase change occurs, there is:

$$\dot{m}^+=\frac{\rho_v\rho_l}{\rho}\alpha_v(1-\alpha_v)\frac{3}{R_b}\sqrt{\frac{2}{3}\frac{\max(p_v-p,0)}{\rho_l}} \tag{6}$$

$$\dot{m}^-=\frac{\rho_v\rho_l}{\rho}\alpha_v(1-\alpha_v)\frac{3}{R_b}\sqrt{\frac{2}{3}\frac{\max(p-p_v,0)}{\rho_l}} \tag{7}$$

Among them, $\dot{m}^+$ represents the evaporation process, $\dot{m}^-$ represents the condensation process, R_b is the radius of the cavity and p_v is the saturation vapor pressure at the local temperature. The calculation formula of the cavity radius is

$$R_b = \left[\frac{\alpha_v}{(1-\alpha_v)}\frac{3}{4\pi}\frac{1}{N_b}\right]^{1/3} \tag{8}$$

where $N_b = 10^{13}\ \mathrm{m}^{-3}$ is the cavity number density.

1.3 *Third-generation vortex identification method*

Vorticity does not represent fluid rotation because the effects of deformation should also be considered. Larger vorticity does not necessarily cause strong rotations, and small vorticity may also cause strong rotations.

The third generation vortex identification technology uses the ratio of vorticity and deformation to define the vortex boundary. $\boldsymbol{\Omega}_R$ is defined as belows

$$\boldsymbol{\Omega}_R = \frac{\|\boldsymbol{B}\|_F^2}{\|\boldsymbol{A}\|_F^2 + \|\boldsymbol{B}\|_F^2} = \frac{b}{a+b} \tag{9}$$

where $a = \|\boldsymbol{A}\|_F^2$, $b = \|\boldsymbol{B}\|_F^2$. To prevent the appearance of unphysical vortices, a small value ε is added to the denominator, as shown below.

$$\boldsymbol{\Omega}_R = \frac{b}{a+b+\varepsilon} \tag{10}$$

For $\boldsymbol{\Omega}_R$, increasing or decreasing the threshold values does not affect the vortex structure. However, a higher threshold value is needed if the position of the vortex core is desired, such as 0.8, 0.9, etc.

1.4 *FW-H formulation*

Here we use the most widely used and universally significant Farassat Formulations 1A formulation. The derivation process is omitted here. Its integral expression is given as follows:

$$4\pi p_T'(x,t) = \int_{f=0}\left[\frac{\rho_0 \dot{v}_n}{r(1-M_r)^2} + \frac{\rho_0 v_n \hat{r}_i \dot{M}_i}{r(1-M_r)^3}\right]_{\mathrm{ret}} \mathrm{d}S + \int_{f=0}\left[\frac{\rho_0 c v_n (M_r - M^2)}{r^2(1-M_r)^3}\right]_{\mathrm{ret}} \mathrm{d}S \tag{11}$$

$$4\pi p_L'(x,t) = \int_{f=0}\left[\frac{\dot{p}\cos\theta}{cr(1-M_r)^2} + \frac{\hat{r}_i \dot{M}_i p\cos\theta}{cr(1-M_r)^3}\right]_{\mathrm{ret}} \mathrm{d}S + \int_{f=0}\left[\frac{p(\cos\theta - M_i n_i)}{r^2(1-M_r)^2} + \frac{(M_r - M^2)p\cos\theta}{r^2(1-M_r)^3}\right]_{\mathrm{ret}} \mathrm{d}S \tag{12}$$

Here p_T' stands for thickness noise, p_L' stands for load noise, $(x,t)(y,t)$ are the space-time variables of the observation point and the sound source respectively, r is the norm of the vector radius from the observation point to the sound source, $\hat{r}_i$ represents the normalization of the vector radius, M_r is the sound source Mach number in the satellite coordinate system, $1-M_r$ is called the Doppler factor, $\dot{v}_n$ represents the derivative of the speed to the sound source time, $\cos\theta$ is the vector path from the observation point to the sound source, $[\ ]_{\mathrm{ret}}$ is retarded time, which represents the satellite coordinates after considering the Doppler effect.

2. Numerical setup and verification

The DTMB 4119 propeller (three-blade) is selected as the research object. The basic parameters of the propeller are shown in Table 1.

Table 1 DTMB 4119 propeller geometry model parameters

Diameter/m	Blades number	Skew/°	Rake/°	Blade section	Rotation direction
0.1	3	0	0	NACA66, $a=0.8$	Right

The cylindrical computational domain is selected here. The diameter of domain is $D_C = 3D$. The diameter of AMI surface is $D_A = 1.2D$. $L = 6D$ represents the entire length of domain. The incoming flow flows along the positive y-axis direction. The outlet surface is $L_2 = 4D$ away from the propeller, as is shown in Fig. 1.

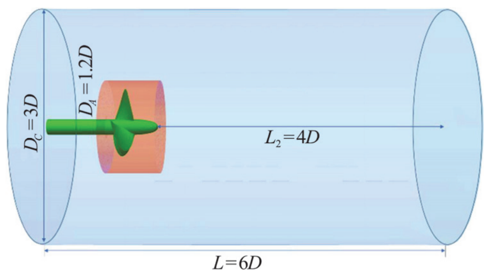

Fig. 1 (Color online) Numerical domain for DTMB4119 propeller

An unstructured mesh is used in this example. The total number of grids is about 3.45×10^{6}. Figure 2 shows the mesh distribution on the propeller surface. The calculation time step is set as 10^{-5}. The Courant number keeps less than 1 during the whole process. The noise signal is sampled with frequency equal to the time step. Crank Nicolson format is selected for computing time derivative. The spatial divergence is in Guass upwind format.

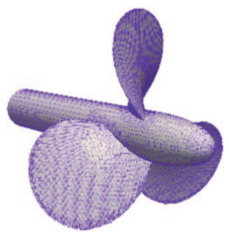

Fig. 2 (Color online) Local mesh for DTMB4119 propeller

In order to verify the result convergence, the thrust coefficient and torque coefficient are compared with the experiments under different advance coefficients. As shown in Fig. 3, the results show that the simulation is relatively accurate in this case.

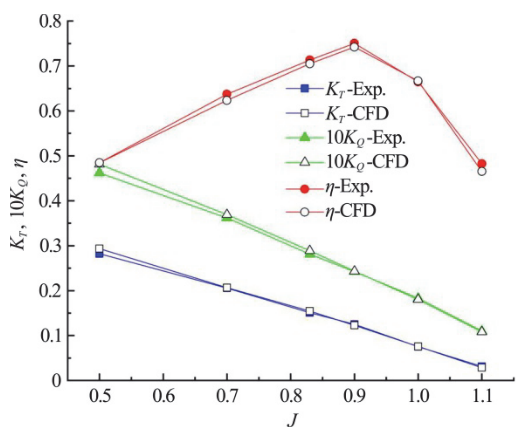

Fig. 3 (Color online) Predicted force coefficients compared with experiment[21]

A non-cavitation and cavitation working conditions are selected separately in this paper. In order to compare the effects of different vortex identification techniques on the flow field and sound field for propeller's wake. The relevant parameters of the two working conditions are shown in Table 2.

Table 2 Working condition parameters with or without cavitation

Parameters	Without cavitation	With cavitation
Max inlet velocity	5 m/s	15 m/s
Rotate speed	25.2 r/s	66.7 r/s
Saturation pressure	-	2 300 Pa

3. Vortex field analysis

3.1 *Non-cavitation vortex field*

Three streamwise sections are selected from upstream to downstream, and their vortex field is extracted for analysis. The y-coordinates of these sections are $-0.25D$, $0.5D$ and $1D$ separately, with 1 located upstream of the propeller and 2 located downstream. For the convenience of distinction, The labels I, II, III are used to represent them. Three kinds of vortex identification technologies, vorticity, Q-criterion and Ω_R, are employed to compare the details of the vortex results. The cloud map on each section is time-averaged during one rotation period.

Figure 4 shows the cloud map of y vorticity component. It can be seen that the vorticity upstream is smaller than that of the downstream. Vorticity is an essential property in viscous fluids, and its capture accuracy is affected by grid accuracy seriously. The vorticity upstream is almost not captured, due to the coarse mesh upstream of the propeller. This means that eddies cannot be finely captured by the first-generation vortex identification technology.

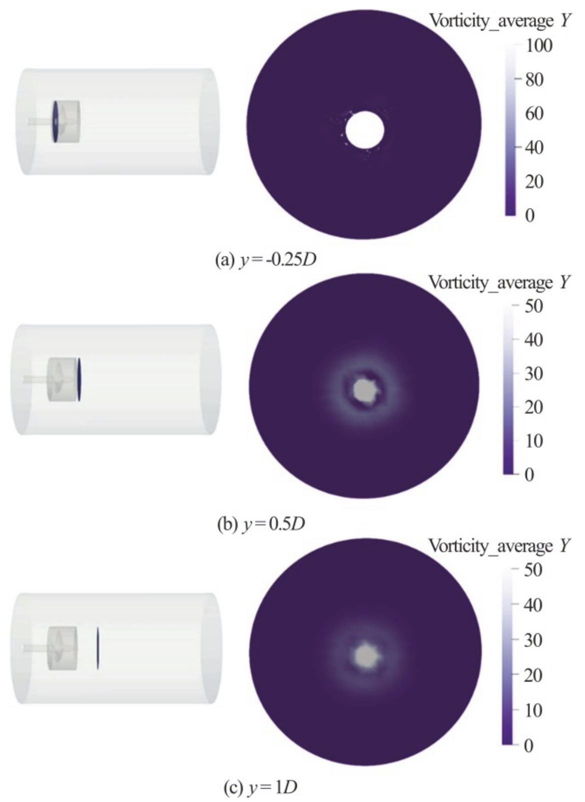

Fig. 4 (Color online) Time-averaged vorticity cloud map in three planes for non-cavitation condition, remembered as I, II and III

The vorticity value increases gradually as the section position moves downstream. However, the vortex core at the hub center is indistinct (see II, III sections), and only a vague range is shown relatively. Since the III section is located further downstream, the vorticity is less obvious compared with the II section.

In conclusion, vorticity is sensitive to the fineness of the mesh, and decays rapidly and as the section position moves downstream. From these perspectives, the first-generation vortex identification method has many deficiencies in capturing propeller wake vortices in the non-cavitation state.

Figure 5 shows the cloud map of the Q-criterion. The definition of Q-criterion is

$$Q=\frac{1}{2}(\tilde{\Omega}_{ij}\tilde{\Omega}_{ij}-\tilde{S}_{ij}\tilde{S}_{ij}) \tag{13}$$

Here $\tilde{\Omega}_{ij}$ and $\tilde{S}_{ij}$ denote the antisymmetric and symmetric parts of the velocity gradient tensor, respectively. $Q>0$ means that the rotation rate of the fluid in this region is greater than the strain rate, and the flow vortex structure is dominant at this time.

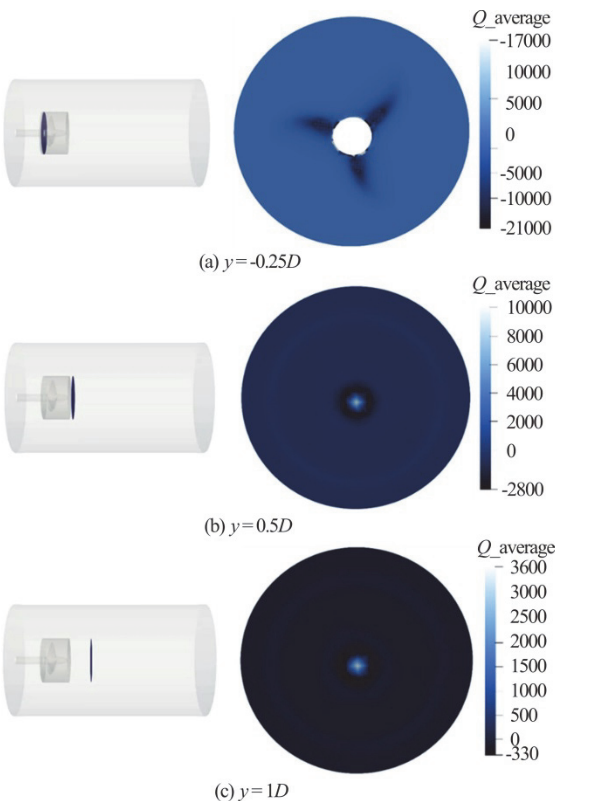

Fig. 5 (Color online) Time-averaged Q-criterion cloud map in three planes for non-cavitation condition, remembered as I, II and III

Figure 5 shows the Q value distribution in sections. It can be seen that the Q-criterion captures the vortices distribution upstream better, as shown by section I. This may be due to the small range of Q in the color bar, making the vortex more obvious.

Compared with the first-generation vortex identification technology, the Q-criterion improves the clarity of the hub vortex core at II, III sections downstream. However, it also has disadvantages, that is, the outer vortices are not captured on Section III. Although a faint vortex ring can be seen on Section II.

Compared with the first generation, the second-generation vortex identification technology is more accurate in replicating the hub vortex core of the propeller. However, it also has the problem of "unclear far-field vortex capture downstream", like the first-generation vortex identification technology.

Figure 6 shows the distribution contours of the third-generation vortex identification technology, Ω_R, at three cross-sections. Compared with the first two vortex identification technologies, Ω_R displays the annular distribution of vorticity better on the downstream sections, and its detail is far more than the first two vortex identification technologies. Moreover, the vortex is clearly captured even at the far downstream position of section III. It reflects the great advantage of the third-generation vortex identification technology in simulating the wake of a non-cavitation propeller.

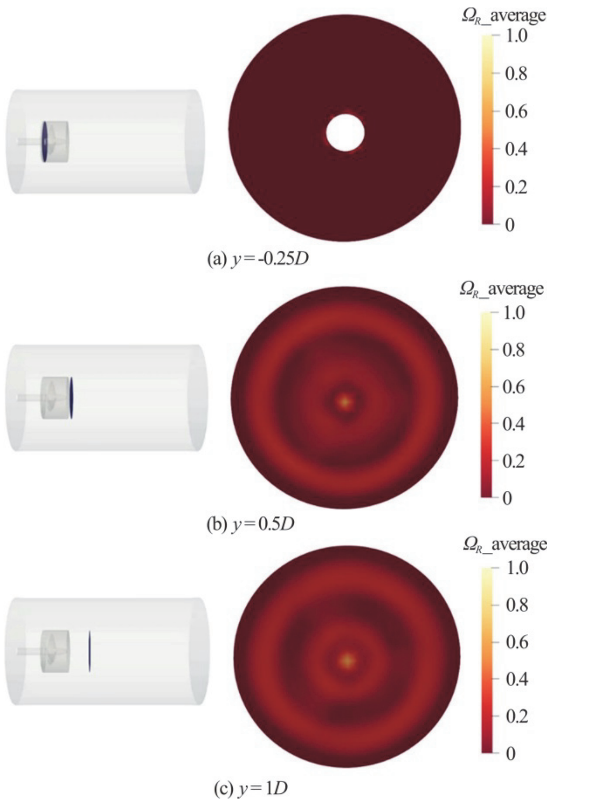

Fig. 6 (Color online) Time-averaged Ω_R cloud map in three planes for non-cavitation condition, remembered as I, II and III

It can be seen that for non-cavitation propellers, the third-generation vortex identification technology overcomes the defects of grid sensitivity, incomplete capture of downstream vortices, and inconspicuous vortex cores. It represents non-cavitation propellers wake vortices better.

Figure 7 shows the 3-D contour of the vortex structure in the wake. It can be seen that the vortex structure drawn by the Q-criterion is sensitive to the value. When $Q = 500$, the vortex length is reduced significantly compared with that of $Q = 100$. However, the third-generation vortex identification technology does not have such problem. In fact, the contour of the vortex hardly changes with Ω_R between 0.3-0.8. This demonstrates the robustness of the third-generation vortex identification technology.

It can also be seen from Fig. 7 that the vortex structure described by the Q-criterion has false vortex signals near the propeller hub, as shown by the black box in the figure. The vortices drawn by Ω_R do not have such problems. This shows that the third-generation vortex identification technology can remove non-physical vortex components in simulating non-cavitation propeller wake vortices, making the vortex field closer to real physics.

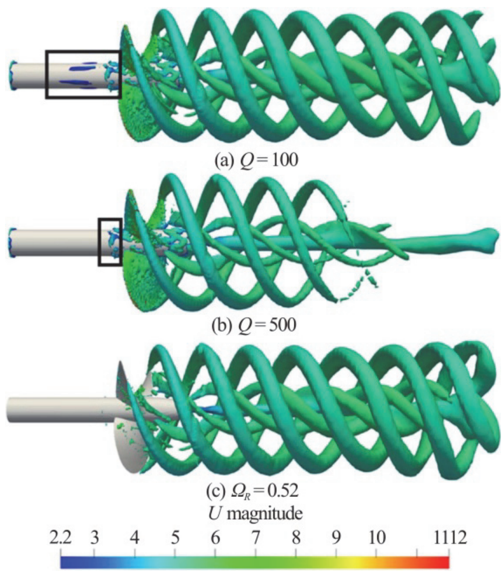

Fig. 7 (Color online) Instantaneous cloud image of propeller wake vortex in non-cavitation state: The black boxes denote the spurious vortex area according to Q-criterion

3.2 *Cavitation vortex field*

The previous section is for non-cavitation conditions. This section will analyze the cavitation conditions.

In cavitation conditions, the incoming flow speed is faster and the rotating speed is higher. When the velocity reaches a certain amount, the local pressure near the propeller will be lower than the saturation pressure (Bernoulli equation), then the water will vaporize, resulting in cavitation. Cavitation is a specific phenomenon of hydrodynamics, which causes various negative effects on noise and interacts with vortices. Experiments revealed that once cavitation occurs, it will become the main noise source. Therefore, it is necessary to study cavitation conditions. Similar to the previous section, for cavitation conditions, this section also analyzes the applicability of the third-generation vortex identification technology to propeller wakes in cavitation conditions from the vortex cloud images on the three sections I, II and III.

Figure 8 shows the vortices distribution using the first-generation vortex identification technology. Compared with the non-cavitation state, the vorticity of the cavitation is enhanced obviously. The vortex capture effect at the upstream section I is better than that in the non-cavitation condition. However, there are still discontinuities and other problems. It can be seen that the vortex core is even less obvious at the downstream section III. The fuzzy phenomenon still exists for downstream far-field vorticity.

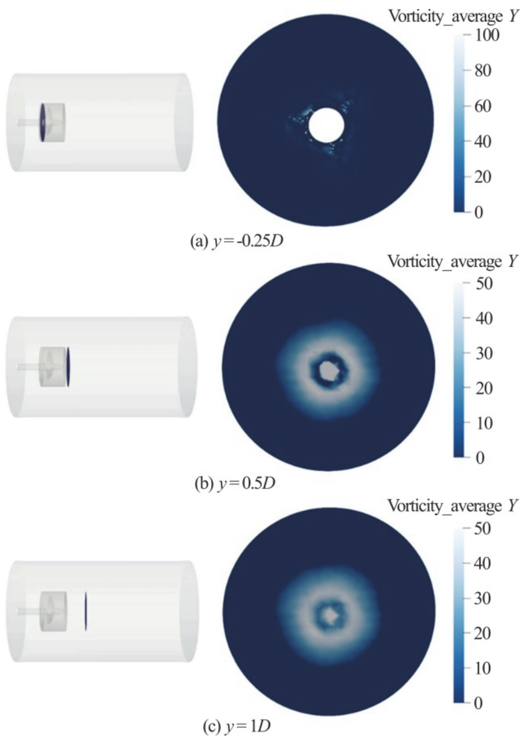

Fig. 8 (Color online) Time-averaged vorticity cloud map in three planes for cavitation condition, remembered as I, II and III

Figure 9 shows the vortices distribution of the second-generation vortex identification technology Q. Compared with vorticity, the vortex captured at the upstream section I is clearer. However, the fuzzy phenomenon still exists for the downstream vortex core.

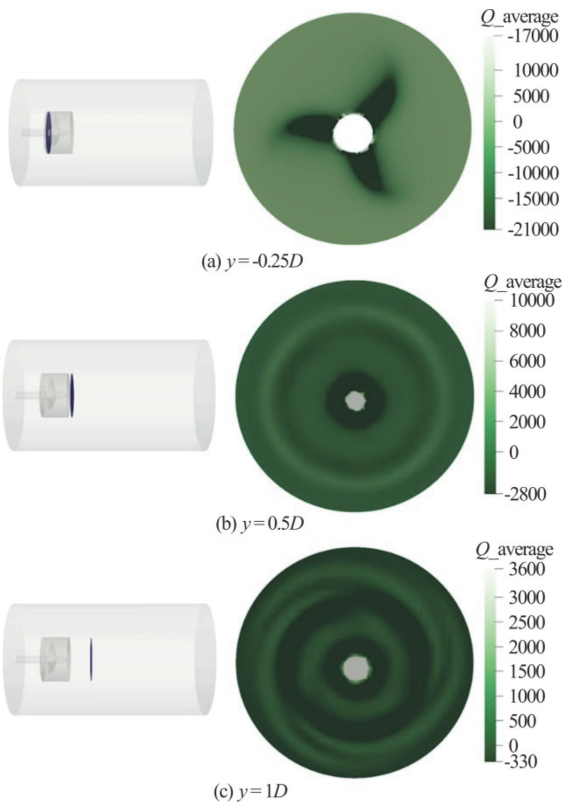

Fig. 9 (Color online) Time-averaged Q-criterion cloud map in three planes for cavitation condition, remembered as I, II and III

However, it can be seen that there is a clear distinction between the strong and weak bands of vortices, which is an improvement compared to the first-generation vortex identification technology. The helical structure at section III seems to be inconsistent with the physical reality, which may be caused by the spurious numerical vortex signal generated by the Q-criterion.

The vortices cloud map of the third-generation vortex identification technology is shown in Fig. 10. Since the vortices distribution is denser in the cavitation state, more vortex rings can be seen on section II. Compared with the first two vortex identification technologies, it is obvious that Ω_R can capture the denser vortex rings of the cavitation propeller in more detail. In addition, through the distribution of section III, it can be found that Ω_R reproduces the fine vortices more clearly in the downstream far field than the first two kinds of vortex identifications.

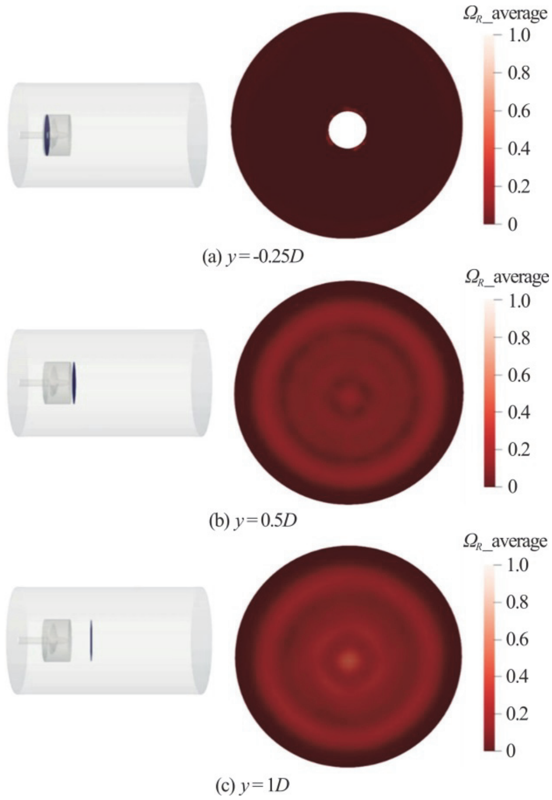

Fig. 10 (Color online) Time-averaged vorticity cloud map in three planes for cavitation condition, remembered as I, II and III

Figure 11 shows the 3-D vortices iso-surface of the cavitation propeller for Q, Ω_R. Different from the non-cavitation state, the vortices drawn by Q-criterion has a large number of false signals near the wall. This problem does not exist for the third-generation vortex identification technology. In addition, like the non-cavitation state, the vortex distribution plotted by the Q-criterion is severely affected by the value, and the vortices range of $Q=500$ is significantly smaller than that of $Q=100$. However, Ω_R does not have this problem.

In conclusion, for the cavitation propeller wake, the first-generation vortex identification technology has problems such as discontinuous capture of the vortex ring and unclear downstream vortices. False vortices signals will appear near the wall when using the second-generation vortex identification technology, and the vortex distribution range is sensitive to the Q value. The third-generation vortex identification technology can overcome the above problems, and has great advantages in propeller wake vortex simulation in cavitation conditions.

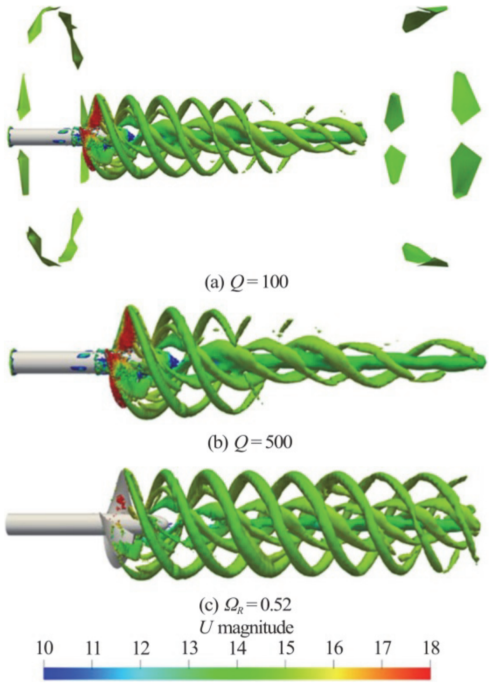

Fig. 11 (Color online) Instantaneous cloud image of propeller wake vortex in cavitation state

4. Acoustic field analysis considering vortex

4.1 *Hydrophone positions*

In this chapter, acoustic analogy will be used to predict the propeller noise under non-cavitation and cavitation conditions, and the nonlinear sound source will be linked with the vortex field to explain the distribution law.

In order to study the sound field distribution, several probes are set up in the near field and far field respectively. Four test points are set in the near field, named as N_1, N_2, N_3, N_4 from upstream to downstream sequentially, as shown in Fig. 12. The four hydrophones are all at a height of $0.8D$ above the centerline of the propeller, and the spacings are $0.2D$, $0.4D$ and $0.4D$ subsequently. Among them, N_2 test point is located above the propeller blades.

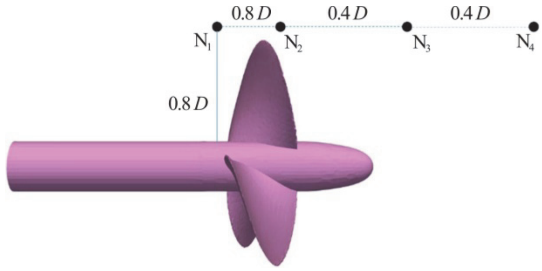

Fig. 12 (Color online) Near field hydrophone positions

Four sets of probes are set up in the far field, two of which are located on the $y = 0$ plane and $y = -3D$ plane, which are denoted as y_0, y_1 planes respectively. The other two groups are located in the $z = 0$ plane, $z = -3D$ plane, denoted as z_0, z_1 respectively. As shown in Fig. 13, the four groups of far-field probes are all around the center of the propeller, with a radius of $10D$. Each group has a total of 36 probes with one hydrophone every 10°.

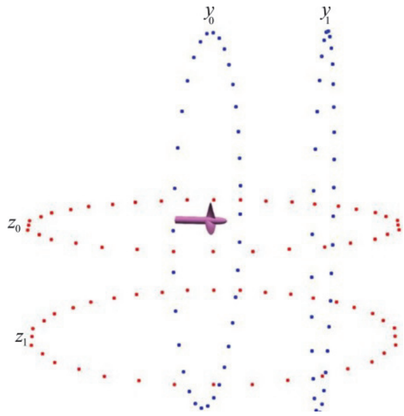

Fig. 13 (Color online) Far field hydrophone positions

4.2 *Non-cavitation acoustic field*

The monopole component (load noise) and dipole component (thickness noise) are extracted respectively in the near field. The acoustic characteristics of the non-cavitation propeller are analyzed, as shown in Fig. 14.

It can be seen that the dipole sound pressure is much larger than that of the monopole, and its period is about 1/3 of the monopole. This is in line with the physical reality. Because the DTMB4119 propeller is three-blade, and the dipole component is related to the change of the blade surface pressure. Therefore, every time a blade turns, the dipole sound goes through a cycle. The monopole is related to the rotational motion of the propeller, so it takes one cycle for the propeller to rotate once.

At the same time, it can be seen that the sound pressure value of N_2 is the largest, followed by N_1, N_3 and N_4. This is easy to explain. Because N_2 is the closest to the propeller blades. The sound pressure value is negatively correlated with the distance whether it is a monopole or a dipole. Therefore, the sound pressure gradually decreases. However, it is worth noting that the dipole decreases more rapidly with distance. And there is an obvious time delay effect at each point predicted by the dipole, while such effect of the monopole does not exist. This is because the prediction of monopoles adopts the assumption of spherical wave propagation and ignores the propagation time.

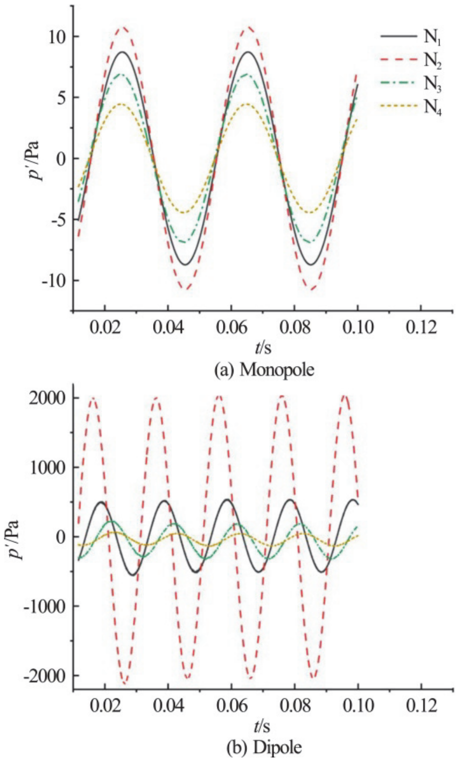

Fig. 14 (Color online) Near-field sound pressure time history in non-cavitation state

To compare the far-field sound pressure characteristics, overall sound pressure level (OASPL) is calculated for each hydrophone in far field. The formula for OASPL is:

$$E = \int S(f)\mathrm{d}f \tag{14}$$

$$\mathrm{OASPL} = 10\lg(E) \tag{15}$$

OASPL of the far-field probes on each plane under non-cavitation conditions is plotted as shown in Fig. 15. It can be seen that the y-plane exhibits obvious isotropic uniformity. This is because the y-direction is in streamwise. Therefore, the OASPL at all angles is roughly the same. However, the z-plane exhibits quadrupole-like properties. It is the result of a combination of monopoles and dipoles. At the same time, it can be seen that the OASPL gradually decreases with the increase of the propeller distance no matter in the y-direction or the z-direction, and the decrease in the two directions is similar.

Although the nonlinear sound of the propeller is not computed in this paper, the cloud map of the nonlinear source can be drawn and its connection with the vortices distribution is analyzed. As shown in Fig. 16, the upper and lower images are the snapshots of Lighthill's sound source and the third-generation vortex identification technology Ω_R respectively at $t = 0.1\ \mathrm{s}$. It can be seen that the extension range of the nonlinear sound source is roughly the same as that of the vortex, which confirms that the vortex is the main source of the nonlinear noise.

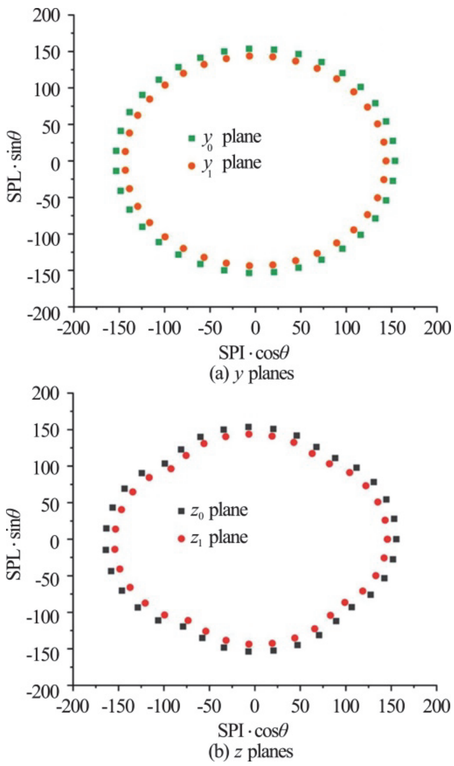

Fig. 15 (Color online) Far-field OASPL in different directions in non-cavitation state

4.3 *Cavitation acoustic field*

Similar to the noise analysis in the non-cavitation condition, the monopole and dipole components are also extracted as the basis for the near-field analysis in cavitation conditions. As shown in Fig. 17, the monopole noise is enhanced compared with the non-cavitation conditions, while the dipole noise is weakened. This may be due to the presence of phase transitions in cavitation, resulting in changes in density and enhances monopole noise. The cavity attached to the blades reduces the pressure fluctuation on the surface, causing the dipole sound reduced.

The far-field acoustic directivity is shown in Fig. 18. It is easy to see that the attenuation speed in the cavitation state is slower than that in the non-cavitation state, whether it is the y-plane or the z-plane. This shows that the acoustic energy in cavitation conditions is stronger. Consistent with the non-cavitation state, the acoustic directivity in cavitation exhibits monopole and quadrupole shapes in the y-, z- planes, respectively.

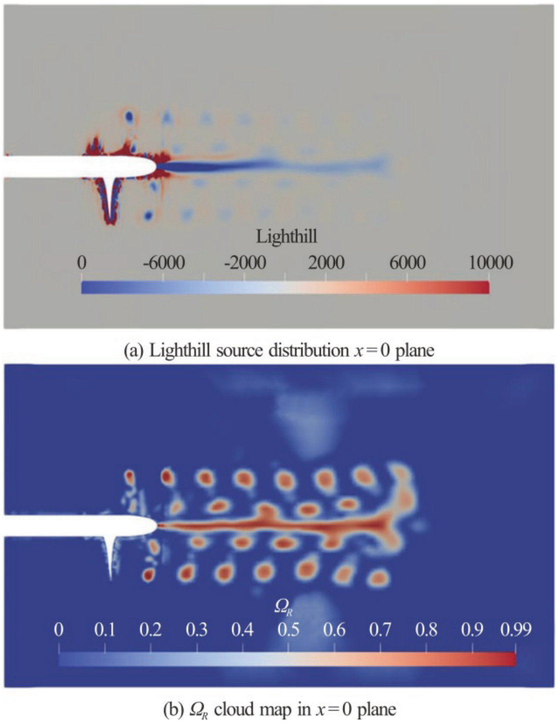

Fig. 16 (Color online) Lighthill sound source distribution and its connection with vortex field in non-cavitation state

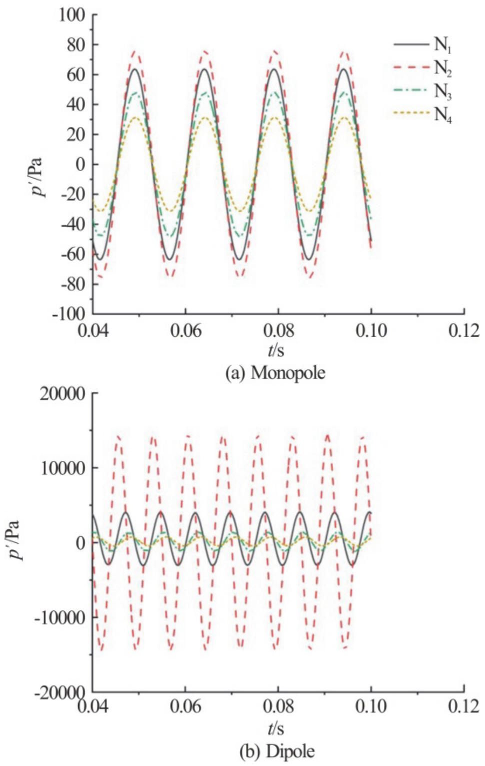

Fig. 17 (Color online) Near-field sound pressure time history in cavitation state

Comparing the nonlinear sound source with the vortices cloud map based on the third-generation vortex identification technology, it can be found that there is a clear correlation between the two as shown in Fig. 19. Precisely, the extended range of the Lighthill source is in line with that of Ω_R, which is even more sensible than the non-cavitation state.

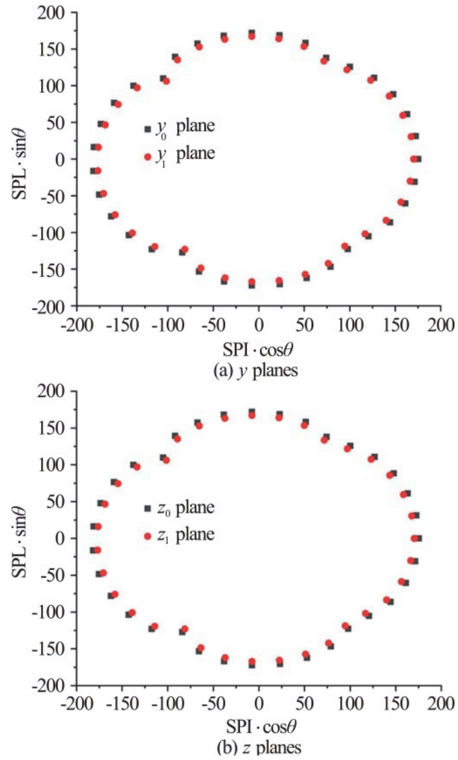

Fig. 18 (Color online) Far-field OASPL in different directions in cavitation state

5. Conclusions

The three-blade propeller DTMB4119 is taken as the research object in this paper. The open source toolkit OpenFOAM is used to simulate flow field and predict underwater noise. DDES turbulence model and the Schnerr-Sauer cavitation model are adopted for flow field simulation. The sound prediction is completed by FW-H formulation. The accuracy of the propeller test example is verified by thrust coefficients, etc. Based on it, three vortex identification technologies are used to analyze the propeller wake vortex characteristics in non-cavitation and cavitation states. The relationship between vortex and sound is studied. Conclusions are drawn as follows:

(1) For non-cavitation propellers, the third-generation vortex identification technology overcomes the defects of grid sensitivity, incomplete capture of downstream vortices, and inconspicuous vortex cores. Compared with vorticity, Q, Ω_R represents the vortex structure better.

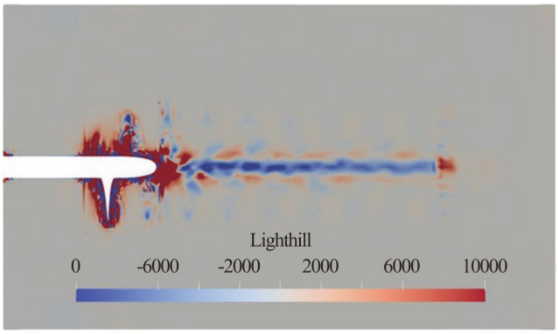

(a) Lighthill source distribution $x = 0$ plane

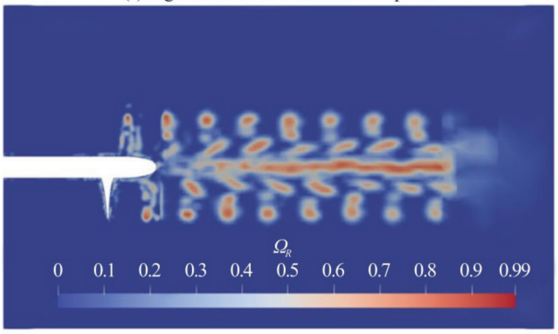

(b) Ω_R cloud map in $x = 0$ plane

Fig. 19 (Color online) Lighthill sound source distribution and its connection with vortex field in cavitation state

(2) For cavitation propellers, vorticity shows problems such as discontinuous capture of the vortex ring and blurred downstream vortices. Q - criterion produces false vortex signals near the wall, and range is sensitive to the Q value. The third-generation vortex identification technology overcomes the above problems, and shows advantages in wake vortices simulation in cavitation conditions.

(3) The distribution of nonlinear sound source is related to vortices, and the third-generation vortex identification technology accurately predicts the range of vortex and maintains a good consistency with the Lighthill tensor distribution.

References

[1] Liu C. New ideas on governing equations of fluid dynamics [J]. *Journal of Hydrodynamics*, 2021, 33(4): 861-866.

[2] Dong X., Hao C., Liu C. Correlation between vorticity, Liutex and shear in boundary layer transition [J]. *Computers and Fluids*. 2022, 238: 105371.

[3] Yu Y., Shrestha P., Alvarez O. et al. Investigation of correlation between vorticity, Q, λ_{ci}, λ_2, Δ and Liutex [J]. *Computers and Fluids*, 2021, 225: 104977.

[4] Liu C., Gao Y. S., Dong X. R. et al. Third generation of vortex identification methods: Omega and Liutex/Rortex based systems [J]. *Journal of Hydrodynamics*, 2019, 31(2): 205-223.

[5] Dong X., Gao Y., Liu C. New normalized Rortex/vortex identification method [J]. *Physics of Fluids*, 2019, 31(1): 011701.

[6] Wang Y. Q., Gao Y. S., Liu J. M. et al. Explicit formula for the Liutex vector and physical meaning of vorticity based on the Liutex-Shear decomposition [J]. *Journal of Hydrodynamics*, 2019, 31(3): 464-474.

[7] Gao Y. S., Liu J. M., Yu Y. et al. A Liutex based definition and identification of vortex core center lines [J]. *Journal of Hydrodynamics*, 2019, 31(3): 445-454.

[8] Cianferra M., Petronio A., Armenio V. Non-linear noise from a ship propeller in open sea condition [J]. *Ocean Engineering*. 2019, 191: 106474.

[9] Ebrahimi A., Seif M. S., Nouri-Borujerdi A. Hydrodynamic and acoustic performance analysis of marine propellers by combination of panel method and FW-H equations [J]. *Mathematical and Computational Applications*, 2019, 24(3): 81.

[10] Wu Q., Huang B., Wang G. et al. Numerical modelling of unsteady cavitation and induced noise around a marine propeller [J]. *Ocean Engineering*, 2018, 160: 143-155.

[11] Viitanen V. M., Hynninen A., Sipilä T. et al. DDES of wetted and cavitating marine propeller for CHA underwater noise assessment [J]. *Journal of Marine Science and Engineering*, 2018, 6(2): 56.

[12] Lighthill M. J. On sound generated aerodynamically I. General theory [J]. *Proceedings of the Royal Society of London. Series A. Mathematical and Physical Sciences*, 1952, 211(1107): 564-587.

[13] Curle N. The influence of solid boundaries upon aerodynamic sound [J]. *Proceedings of the Royal Society of London. Series A. Mathematical and Physical Sciences*, 1955, 231(1187): 505-514.

[14] Ffowcs Williams J. E., Hawkings D. L. Sound generation by turbulence and surfaces in arbitrary motion [J]. *Philosophical Transactions of the Royal Society of London. Series A, Mathematical and Physical Sciences*, 1969, 264(1151): 321-342.

[15] Ianniello S., Muscari R., Di Mascio A. Ship underwater noise assessment by the acoustic analogy. Part I: Nonlinear analysis of a marine propeller in a uniform flow [J]. *Journal of Marine Science and Technology*, 2013, 18(4): 547-570.

[16] Ianniello S., Muscari R., Di Mascio A. Ship underwater noise assessment by the Acoustic Analogy part II: Hydroacoustic analysis of a ship scaled model [J]. *Journal of Marine Science and Technology*, 2014, 19(1): 52-74.

[17] Choi W. S., Choi Y., Hong S. Y. et al. Turbulence-induced noise of a submerged cylinder using a permeable FW–H method [J]. *International Journal of Naval Architecture and Ocean Engineering*, 2016, 8(3): 235-242.

[18] Lloyd T., Rijpkema D., van Wijngaarden E. Marine propeller acoustic modelling: comparing CFD results with an acoustic analogy method [C]. *Fourth International Symposium on Marine Propulsors*, Austin, Texas, USA, 2015.

[19] Spalart P., Allmaras S. A one-equation turbulence model for aerodynamic flows [C]. *30th Aerospace Sciences Meeting and Exhibit*, Reno, NV, USA, 1992, 439.

[20] Schnerr G. H., Sauer J. Physical and numerical modeling of unsteady cavitation dynamics [C]. *Fourth International Conference on Multiphase Flow*, Los Angeles, USA, 2001.

[21] Jessup S. D. An experimental investigation of viscous aspects of propeller blade flow [R]. Washington DC, USA: The Catholic University of America, 1989.